

# Estimation of Stability Derivatives Due to Translational Motion of Various LTA Vehicles Using CFD



Anoop Sasidharan, Ratna Kishore Velamati, Sheeja Janardhanan,  
Venkata Ramana Murthy Oruganti, and Akram Mohammad

## 1 Introduction

Wind data is an inevitable part of the wind energy sector. The major applications of wind data are the dispatching of load [1], forecasting demand [2], planning the generation [3] and maintenance of the mechanical structures [4]. The conventional method of wind data collection in the wind energy harvesting sites is based on the pole based methods. This method has a few drawbacks, such as the need for a permanent structural setup which may cause environmental and aesthetic impacts on the site, the inability to vary the altitude of the structure, a long gestation period and cannot be relocated or reused easily [5]. A tethered aerostat can be considered as an alternate method for low-altitude wind measurement. Compared to the conventional method, the proposed method has the following advantages; it gives freedom to vary the altitude of operation, it does not require any permanent structure for the deployment, takes less time for deploying at a site and can be relocated easily to different locations and reused. The feasibility of such a system should be investigated with the help of mathematical models.

Mathematical modelling of complex systems such as lighter-than-air (LTA) vehicles plays a vital role in understanding and predicting the unsteady aerodynamic behaviour of that system [6]. Since the functional form of aerodynamic effects [7] in the form of forces and moments on the aerial vehicle is not readily available for

---

A. Sasidharan · R. K. Velamati (✉) · V. R. M. Oruganti  
Department of Electrical and Electronics Engineering, Amrita School of Engineering,  
Coimbatore, Amrita Vishwa Vidyapeetham, Coimbatore, India  
e-mail: [v\\_ratnakishore@cb.amrita.edu](mailto:v_ratnakishore@cb.amrita.edu)

S. Janardhanan  
School of Naval Architecture and Ocean Engineering, Indian Maritime University,  
Visakhapatnam, India

A. Mohammad  
Department of Aerospace Engineering, King Abdulaziz University, Jeddah, Saudi Arabia

direct measurement, mathematical derivatives are needed to model these forces and moments [8, 9]. Derivatives are a measure of the degree of variation of a function or a parameter with respect to input or another parameter. In the field of dynamics, those derivatives that can represent the model's sensitivity to some motion variables are termed stability derivatives because these derivatives help simplify the model so that the stability analysis and control of the model become easy. Aerodynamic models using stability derivatives are considered an accurate approach to the mathematical modelling of aerial vehicles.

The estimation or extraction of the stability derivatives was reported mainly using flight tests, wind tunnel tests and numerical methods. Some of the essential works reported in these classes are presented here. The estimation of the aerodynamic derivatives for the LTA vehicles using a semi-empirical procedure was reported in [10]. They have considered the hull-fin interference using an analytical model and the static wind tunnel data by which the dynamic motion of the vehicle can be represented well. As an extension, they have investigated the longitudinal and lateral stability derivatives for the TCOM 71M aerostat [11]. The model also verified the static and dynamic stability of the aerostat obtained using the stability derivatives. A neural network-based prediction of the dynamic derivatives of an aircraft at high angles of attack was presented by [12]. They provided decent results for pitching moment derivatives compared to the wind tunnel experimental data. A wind tunnel-based stability derivative estimation for a hybrid buoyant aerial vehicle is presented by [13]. They compared the stability of the vehicle with wings and without wings. Even though the physical realism of the experimental methods such as flight tests and wind tunnel tests is highly appreciable, they have some limitations such as scaling errors, blocking effects and high cost. A system identification approach for obtaining the stability derivatives of an LTA vehicle undergoing swing oscillation was presented in [14]. Computational methods were also reported to estimate the stability derivatives of LTA vehicles [15].

Considering the fact that the computational fluid dynamics (CFD) solvers are now capable of handling high-performance tasks due to the developments in digital computing, their application in the extraction of stability derivatives is being largely explored by the research community. Most of the limitations of the experimental method, such as the wind tunnel tests, can be overcome by the CFD based methods. A forced oscillation of the body was used for extracting the stability derivatives. The motion variables other than the oscillating parameter are considered zero as per the linear theory. A forced periodic oscillation is imposed on the respective degree of freedom of the model to calculate the respective dynamic derivative. For example, the moment stability derivative due to the pitch rate can be extracted by imposing a periodic angular oscillation about the lateral axis and centre of the moment [9]. The measured moment response will be used to extract the derivative based on the Fourier series approximation. Such a methodology for estimating stability derivatives using CFD for the Zhiyuan airship is presented in [16]. Stability derivatives involved in the pitch and heave motions of the airship were investigated using forced sinusoidal oscillations. They have presented the effect of the tail fins on stability as well. Stability derivatives prediction for a full aircraft configuration was investigated to represent

the unsteady aerodynamic load on the flight dynamics for transonic speeds and larger angles of attack as in [17, 18]. An investigation of the stability of hybrid airships using the analysis of the stability derivatives was presented by [19]. The added mass and inertia terms extraction for an underwater vehicle were reported in [20]. They have compared their results with the results from an experimental procedure and theoretical results. Using stability derivatives addressed by [21], the aerodynamic shape optimisation considered the derivatives as constraints in the optimisation problem.

The forced sinusoidal oscillation-based stability derivative extraction is the most popular method due to the well developed Fourier theory and the easy practical realisation [22, 23]. There are also works reported with different methodologies, such as the work reported in [24]. The history effect and the actuation of the body using piece-wise velocity functions were the basis of their methodology. Even though the rotational dynamics were not able to capture, the methodology was validated with existing data. A detailed literature review of the existing methodologies for stability derivative extraction using CFD can be found in [25].

In this paper, the authors present the stability derivative estimation of aerostat using CFD-based methodology. Stability derivatives of the aerostat due to translational oscillations are extracted by applying a translational forced sinusoidal oscillation along with the vertical and axial directions. A steady wind condition is considered for the study. As the geometry of the aerostat has a significant influence on the aerodynamic stability, the effect of the aerostat envelope shapes in the context of stability derivatives which is investigated as well. It will also help to understand the methodology's efficacy and generalisation thoroughly. There are many aerostat/airship geometries available in the open literature. The NPL shape has been designed and developed by the National Physical Laboratory for reducing the chances of flow separation [26]. It was achieved by providing a continuous variation in the radius of curvature of the profile. The GNVR shape has been reported to be a low drag profile [26]. Both of these shapes represented a combination of different simple geometries, such as ellipse and parabola. It made them feasible for geometry optimisation. A high-altitude application was reported, which was claimed to have a minimum weight to increase the payload and stability (HAA shape) [27]. All the above-mentioned shapes were proposed for stratospheric operation. A bionic design for the airship has been reported to minimise drag (bionic shape) [28]. It was achieved by imitating the morphological features of an aquatic animal (*Physalia physalis*). Other low drag profiles were also reported for specific applications, such as the Zhiyuan shape [16] and Wang shape [29].

The rest of the paper is structured as follows; Sect. 2 presents the methodology involved in the stability derivative extraction of aerostat using CFD analysis and the various aerostat models used for the analysis. Section 4 presents the numerical simulation setup considered for the current study. Section 5 presents the results obtained from the analysis of the stability derivatives due to the heave and surge oscillations and a comparison of the derivatives among the four aerostats. Finally, Sect. 6 concludes the work with the major findings and the future scope of the study.

## 2 Stability Derivatives Extraction Methodology

In this work, the longitudinal motion of the aerostat is considered. The lateral motion of the aerostat is assumed to be negated by the control surfaces. The motion variables involved in the decoupled linear longitudinal dynamic model are  $u$ ,  $w$  and  $q$ . The longitudinal model of the aerostat can be expressed as [30],

$$\begin{aligned} m_x \dot{u} + (ma_z - \dot{D}_q) \dot{q} &= D_a + D_T + D_g \\ m_z \dot{w} - (ma_x + \dot{L}_q) \dot{q} &= L_a + L_T + L_g \\ J_y \dot{q} + (ma_z - \dot{M}_u) \dot{u} - (ma_x + \dot{M}_w) \dot{w} &= M_a + M_T + M_g \end{aligned} \quad (1)$$

where,  $D_a$ ,  $L_a$  and  $M_a$  are the aerodynamic forces and moment,  $D_T$ ,  $L_T$  and  $M_T$  are the forces and moment due to tethers and  $D_g$ ,  $L_g$  and  $M_g$  are the forces and moment due to buoyancy and gravity.

In the current study, the tether dynamics and the forces due to gravity are not included, and for simplicity, they will be named as external forces ( $F_{\text{ext}}$ ) in the rest of the paper. The aerodynamic part of the longitudinal dynamic model of the aerostat can be represented as follows,

$$\begin{aligned} D_a &= D_e + \dot{D}_u u + \dot{D}_w w + (\dot{D}_q - m_z W_e) q \\ L_a &= L_e + \dot{L}_u u + \dot{L}_w w + (\dot{L}_q + m_x U_e) q \\ M_a &= M_e + \dot{M}_u u + \dot{M}_w w + (\dot{M}_q - ma_x U_e - ma_z W_e) q \end{aligned} \quad (2)$$

where  $W_e$  and  $U_e$  are the component of steady velocity along the vertical and axial direction,  $D_e$ ,  $L_e$  and  $M_e$  are the static drag, lift and moment derivatives,  $\dot{D}_u$ ,  $\dot{L}_u$ ,  $\dot{M}_u$  are the drag, lift, and moment derivatives due to axial velocity,  $\dot{D}_w$ ,  $\dot{L}_w$ ,  $\dot{M}_w$  are the drag, lift, and moment derivatives due to vertical velocity,  $\dot{D}_q$ ,  $\dot{L}_q$  and  $\dot{M}_q$  are the drag, lift and moment derivatives due to pitch.

Thus, Eq. (1) can be expressed in matrix form as given in Eq. (3). The terms with dots are the stability derivatives involved in the longitudinal dynamics of the aerostat.

$$\begin{bmatrix} m - \dot{D}_u & 0 & ma_z - \dot{D}_q \\ 0 & m - \dot{L}_w & ma_x + \dot{L}_q \\ ma_z - \dot{M}_u & ma_x + \dot{M}_w & I_y - \dot{M}_q \end{bmatrix} \begin{bmatrix} \dot{u} \\ \dot{w} \\ \dot{q} \end{bmatrix} = \begin{bmatrix} D_e \\ L_e \\ M_e \end{bmatrix} + \begin{bmatrix} \dot{D}_u & \dot{D}_w & \dot{D}_q - m_z W_e \\ \dot{L}_u & \dot{L}_w & \dot{L}_q + m_x U_e \\ \dot{M}_u & \dot{M}_w & \dot{M}_q - ma_x U_e - ma_z W_e \end{bmatrix} \begin{bmatrix} u \\ w \\ q \end{bmatrix} + F_{\text{ext}} \quad (3)$$

The model variables included in the longitudinal model of the aerostat are  $u$ ,  $w$ ,  $q$ ,  $D$ ,  $L$  and  $M$ . These longitudinal dynamic variables are predominant in the heave, surge and pitch motions of the aerostat. Figure 1a shows the orientation of the aerostat axis, wind direction and the motions considered in this study.

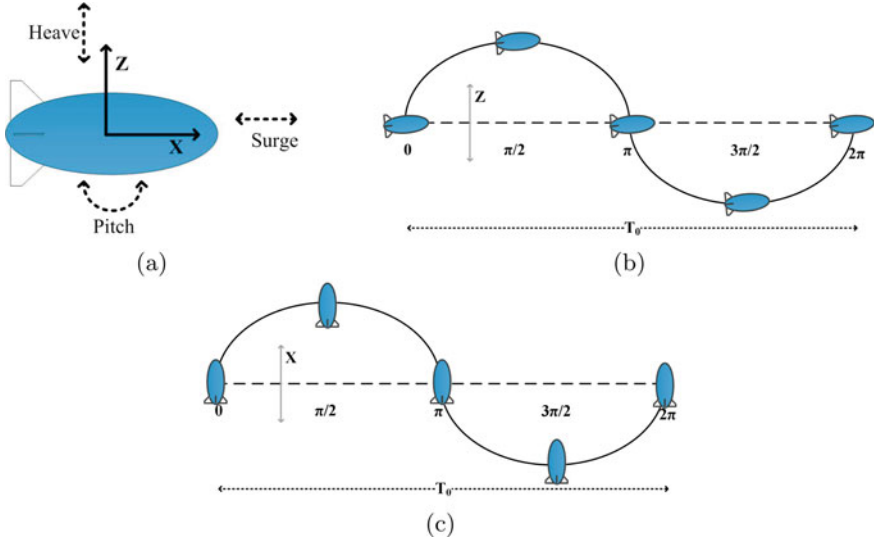


**Fig. 1** a Body fixed reference axis and the directions of motions considered, b heave motion and c surge motion

This paper investigates the stability derivatives due to the surge and heave oscillations of the aerostat. The methodology used for the extraction of the stability derivatives includes the simulation of the model for steady-state and then transient and finally the oscillations in the respective directions. The forces and moment ( $D$ ,  $L$  and  $M$ ) are measured for the oscillated motions. A stable cycle of data will be used from these measured responses to extract the stability derivatives using the Fourier series-based method discussed as follows.

The stability derivatives associated with the translational forward motion (along the  $X$ -axis) can be expressed as the linear decomposed forces and moment as follows,

$$\begin{aligned} D_a^s &= D_e + \dot{D}_u u + \dot{D}_{\dot{u}} \dot{u} \\ L_a^s &= L_e + \dot{L}_u u + \dot{L}_{\dot{u}} \dot{u} \\ M_a^s &= M_e + \dot{M}_u u + \dot{M}_{\dot{u}} \dot{u} \end{aligned} \quad (4)$$

A forced sinusoidal oscillatory motion will be induced in the aerostat axial direction, as shown in Fig. 1b. The motion can be defined by the displacement  $x = u_0 \sin \omega_s t$ , velocity  $u = \omega_s u_0 \cos \omega_s t$  and acceleration  $\dot{u} = -\omega_s^2 u_0 \sin \omega_s t$ . Substituting the values of  $u$  and  $\dot{u}$  into Eq. (4) will result in,

$$\begin{aligned} D_a^s &= D_e + \dot{D}_u \omega_s u_0 \cos \omega_s t - \dot{D}_{\dot{u}} \omega_s^2 u_0 \sin \omega_s t \\ L_a^s &= L_e + \dot{L}_u \omega_s u_0 \cos \omega_s t - \dot{L}_{\dot{u}} \omega_s^2 u_0 \sin \omega_s t \\ M_a^s &= M_e + \dot{M}_u \omega_s u_0 \cos \omega_s t - \dot{M}_{\dot{u}} \omega_s^2 u_0 \sin \omega_s t \end{aligned} \quad (5)$$

As Eq. (5) comprises the sine and cosine components, the coefficients can be compared with the corresponding Fourier series representations of the forces and moment with higher-order terms neglected as given in Eq. (6).

$$\begin{aligned} D_a &= a_0/2 + a_1 \cos \omega_s t + a_2 \sin \omega_s t \\ L_a &= b_0/2 + b_1 \cos \omega_s t + b_2 \sin \omega_s t \\ M_a &= c_0/2 + c_1 \cos \omega_s t + c_2 \sin \omega_s t \end{aligned} \quad (6)$$

By comparing the coefficients of in phase and out of phase components of Eq. (6) and Eq. (5),

$$\begin{aligned} \dot{D}_u &= a_1/(\omega_s u_0); & \dot{L}_u &= b_1/(\omega_s u_0) \\ \dot{M}_u &= c_1/(\omega_s u_0); & \dot{D}_{\ddot{u}} &= -a_2/(\omega_s^2 u_0) \\ \dot{L}_{\ddot{u}} &= -b_2/(\omega_s^2 u_0); & \dot{M}_{\ddot{u}} &= -c_2/(\omega_s^2 u_0) \end{aligned} \quad (7)$$

where,

$$\begin{aligned} a_1 &= \frac{2}{T_0} \int_{-T_0/2}^{T_0/2} D_a(t) \cos(\omega_s t) dt & a_2 &= \frac{2}{T_0} \int_{-T_0/2}^{T_0/2} D_a(t) \sin(\omega_s t) dt \\ b_1 &= \frac{2}{T_0} \int_{-T_0/2}^{T_0/2} L_a(t) \cos(\omega_s t) dt & b_2 &= \frac{2}{T_0} \int_{-T_0/2}^{T_0/2} L_a(t) \sin(\omega_s t) dt \\ c_1 &= \frac{2}{T_0} \int_{-T_0/2}^{T_0/2} M_a(t) \cos(\omega_s t) dt & c_2 &= \frac{2}{T_0} \int_{-T_0/2}^{T_0/2} M_a(t) \sin(\omega_s t) dt \end{aligned}$$

According to Eq. (7), a full cycle response of drag, lift and moment for the forced oscillation along the axial direction will give the six stability derivatives due to axial velocity and acceleration. In a similar manner, the stability derivatives due to heave oscillations can be estimated.

### 3 Aerostat Shapes

In this study, a four-winged aerostat with a '+' orientation of the wings is considered. The length of the aerostat is fixed as 13.5 m by considering the required volume for the desired payload weight. Four different aerostat envelope shapes obtained from the open literature were considered for the comparison of stability derivative results obtained from the current study. They are: the Zhiyuan shape [16], GNVR shape [26], NPL shape [26] and HAA shape [27], as shown in Fig. 2. These shapes were selected by considering the variation of their leading edge geometry, diameter and the

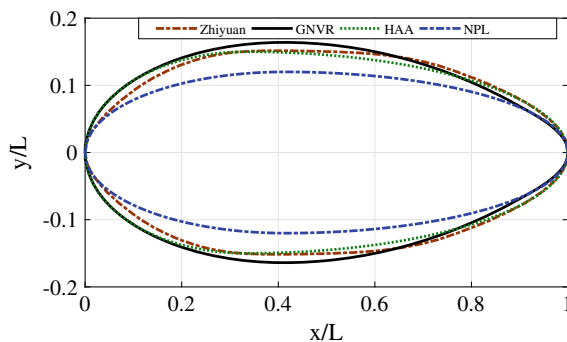


**Fig. 2** Aerostat shapes considered for the current study

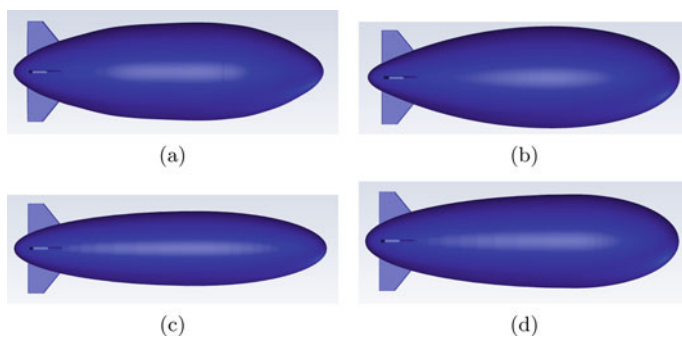


**Fig. 3** Aerostat 3D models; **a** Zhiyuan, **b** GNVR, **c** NPL and **d** HAA shape

lift-drag characteristics. The 3D models used for the simulation analysis are shown in Fig. 3. The maximum diameter is 4.09 m for the Zhiyuan shape, 4.55 m for the GNVR shape, 3.33 m for the NPL shape and 4.09 m for the HAA shape. Among the four aerostat shapes considered, Zhiyuan has the maximum volume, and NPL has the least volume.

## 4 Numerical Simulation

### 4.1 Governing Equations

The current study involves the simulations done using a commercial CFD solver FLU-ENT 20.0. The 3D, incompressible, unsteady flow was solved using the Reynolds Averaged Navier—Stokes (RANS) equations [31]. The governing equations can be expressed as,

$$\nabla \cdot \vec{V} = 0$$

$$\rho \frac{\partial \vec{V}}{\partial t} + \rho \nabla \cdot (\vec{V} \vec{V}) = -\nabla p + \nabla \cdot (\vec{\tau}) + \rho \vec{g} \quad (8)$$

where  $\rho$  is the density,  $\vec{V}$  is the velocity,  $p$  is the pressure and  $\vec{g}$  is the acceleration due to gravity. The stress tensor  $\vec{\tau}$  can be expressed as,

$$\vec{\tau} = (\mu + \mu_t) \left[ \nabla \vec{V} + (\vec{V})^T - \frac{2}{3} \nabla \cdot \vec{V} \mathbf{I} \right]$$

where  $\mu$  is the dynamic viscosity,  $\mu_t$  is the turbulence viscosity and  $\mathbf{I}$  is an identity matrix.

The SIMPLE algorithm was used for the pressure velocity coupling, and the second-order upwind scheme was used for the spatial discretization of the convective terms. A standard interpolation scheme was used for the pressure interpolation, and an iterative time advancement scheme was used for time advancement. The convergence criterion was set to the order of  $10^{-5}$  for continuity, velocity and turbulence quantities.

## 4.2 Computational Domain and Grid

The computational domain used for the simulation is shown in Fig. 4. The dimensions for the domain are selected after an initial domain independence study. The outermost box volume shown in Fig. 4 has a velocity inlet on four faces, a pressure outlet on one face and symmetry on the other. The outer and intermediate volumes were common for all the aerostat simulations presented in this paper. Dimensions of the domain are specified as a function of the aerostat model length. The dynamic mesh feature

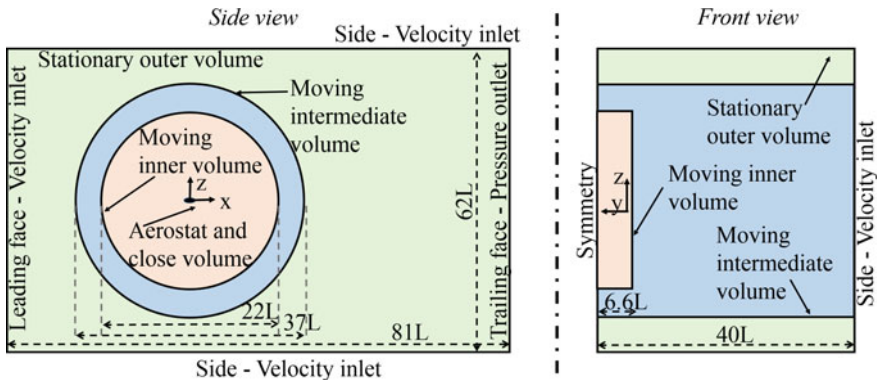
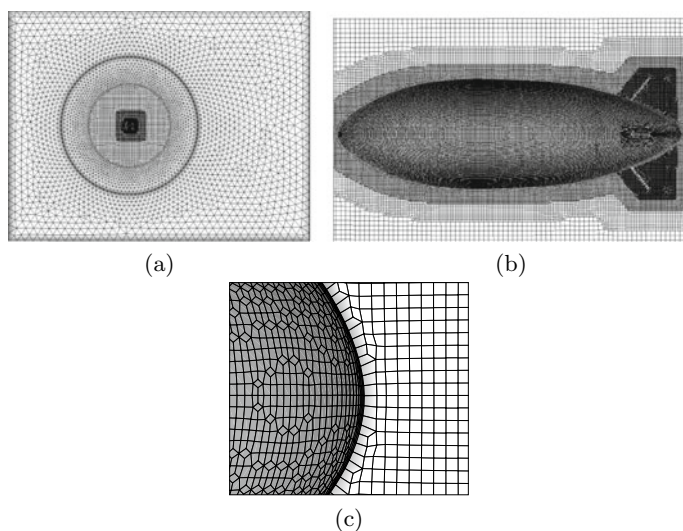


Fig. 4 Computational domain for the current study with the boundary conditions



realised the heave and surge motion simulations. The inner and intermediate volumes were specified as rigid bodies, and the outer volume was kept stationary for the surge and heave motions.

The computational grid used for the current study was made using GAMBIT and FLUENT meshing. The grid for outer and intermediate volumes (refer Fig. 4) was done using GAMBIT with a total of 0.1 M tetrahedral-hexahedral hybrid cells. Comparatively, the coarse grid was used for the outer volumes. Grid for the inner volume with aerostat (different for each aerostat shape) was done using ANSYS FLUENT meshing, as shown in Fig. 5. The range of the number of cells used for each shape is 3–3.5 M. Cut cell mesh topology was used for the inner volumes. The proximity of the aerostat was meshed fine using a refining body of influence in the shape of an ellipse. The inner volume mesh has  $50 \times 50 \times 15$  cells along the  $X$ ,  $Y$  and  $Z$  Cartesian axes. The viscous boundary layer was specified with  $5E - 005$  as the first layer thickness, 1.35 as the stretching ratio and had 18 layers for the aerostat surface. With the above-specified grid configuration, the average value of the wall ' $Y^+$ ' is found to be 0.435 with a minimum of 0.0349 and a maximum of 1.



**Fig. 5** Computational grid; **a** full domain, **b** close to the surface and **c** leading edge section with boundary layers

## 5 Results and Discussion

### 5.1 Grid and Time Step Independence Study

The efficacy of the mesh used for the analysis was tested for different grid refinements, as shown in Fig. 6a, and the simulation time step independence study was performed, as shown in Fig. 6b. The simulation was done by providing the aerostat with an unsteady velocity in the form of a sinusoidal gust. The coefficient of drag and moment was measured respectively for the comparison. The results show that the grid used for the study is independent of the grid refinement and the time step.

### 5.2 Validation of the Grid Motion

The dynamic mesh method for the heave and surge oscillations was validated using the AGARD CT1 [32]. NACA 0012 airfoil was used for the validation. A comparison of the lift coefficient and the pitching moment coefficient with the experimental data is shown in Fig. 7. An appreciable similarity is there with the results, thus validating the grid motion feasibility for further analysis.

### 5.3 Validation of the Stability Derivative Extraction Methodology

The methodology for the extraction of stability derivatives presented in Sect. 2 was validated using the 6:1 prolate spheroid. The added mass coefficients were compared with the theoretical calculation as well as with the simulation study by [16].

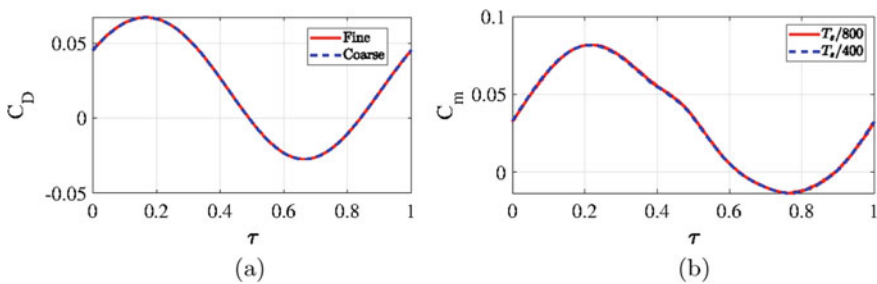


**Fig. 6** **a** Grid independence and **b** time independence test results of the aerostat model

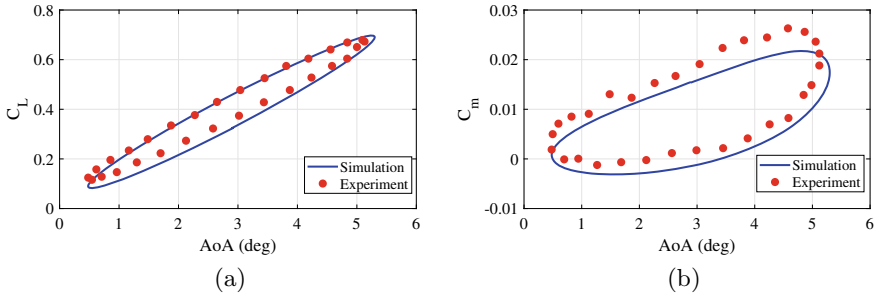


**Fig. 7** Validation of grid motion; **a** lift coefficient and **b** moment coefficient comparison with AGARD CTI

For the estimation of  $\dot{L}_{\dot{w}}$ , a sinusoidal oscillation with amplitude 1 m/s and frequency 3.9 rad was used. For the estimation of  $\dot{M}_{\dot{q}}$ , two sinusoidal oscillations with amplitude  $5^\circ$  and frequencies  $\omega_1 = 29.79$  rad and  $\omega_2 = 21.06$  rad were used.

The theoretical calculations can be obtained using the following equations [33],

$$\dot{L}_{\dot{w}} = -\frac{4}{3}\pi\rho abc \frac{C_0}{2 - C_0} \quad (9)$$

$$\dot{M}_{\dot{q}} = -\frac{4}{15}\pi\rho \frac{abc(a^2 - c^2)^2(A_0 - C_0)}{2(c^2 - a^2) + (C_0 - A_0)(c^2 + a^2)} \quad (10)$$

The simulated value of  $\dot{L}_{\dot{w}}$  is  $-0.0457$  and the theoretical value is  $-0.0430$ , and for  $\dot{M}_{\dot{q}}$ , the corresponding values are  $-0.00339$  and  $-0.0033$ .

#### 5.4 Acceleration and Frequency Independence Study

As the current study involves the forced oscillation of the aerostat along the three degrees of freedom, the independence study of the stability derivatives from the amplitude of oscillations (acceleration of the motion) has to be done. Such a study was conducted for the Zhiyuan aerostat for heave oscillations, and the acceleration independence was tested for all the stability derivatives involved as shown in Fig. 8. The coefficients with almost the same values show the simulation's acceleration independence.

The estimation of moment stability derivatives involves the application of two sinusoidal oscillations with different frequencies. A frequency independence study was conducted for all the stability derivatives that required two frequencies. The results for the estimation of  $\dot{M}_{\dot{q}}$  for a  $10^\circ$  angle of attack are shown in Fig. 9. Here, three frequencies are used for the comparison; 2.32 rad/s (2.7 s), 2.09 rad/s (3 s) and 1.90 rad/s (3.3 s). The frequency independence of the simulation is clearly observable in Fig. 9.

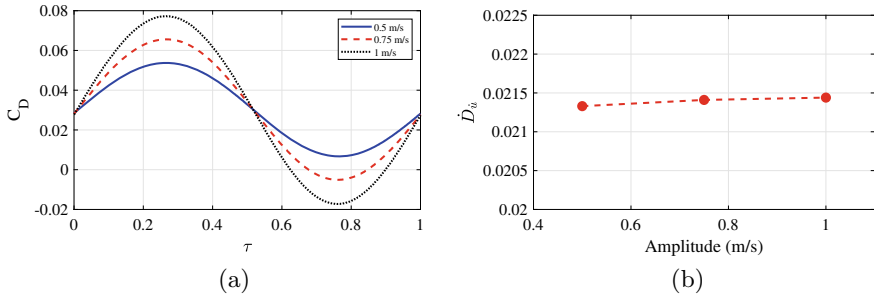


**Fig. 8** Acceleration independence study results; **a** a full cycle drag response and **b** stability derivative,  $\dot{D}_u$ , comparison

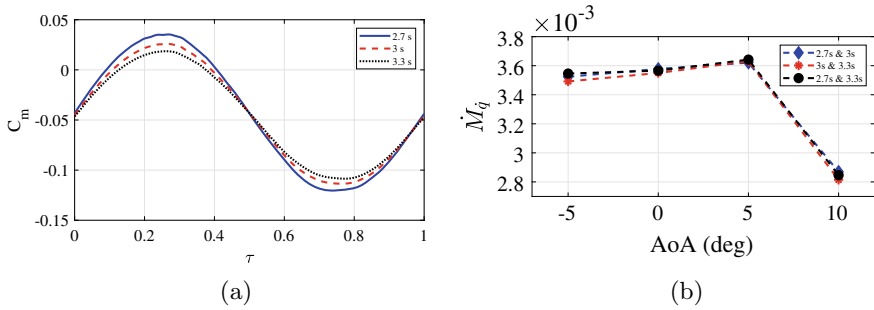


**Fig. 9** Oscillation frequency independence study results; **a** a full cycle moment response and **b** stability derivative,  $M_q$ , comparison

The stability derivative extraction methodology presented in Sect. 2 was applied to the four aerostats with four different angles of attack. Three full cycles of responses were obtained for all the simulation cases, and a full stable cycle was selected for the analysis. The surge and heave oscillations were simulated using an amplitude of oscillation of 1 m/s. The drag, lift and moment response were measured for each aerostat shape for the heave oscillations. All the responses are plotted with the non-dimensional time on the X-axis.

## 5.5 Zhiyuan Aerostat

The response of the Zhiyuan aerostat for surge and heave oscillations is shown in Fig. 10. The figure shows the lift response for the heave oscillation. The first column of the figure represents a continuous set of responses and the second column represents the single-cycle plots that are used for the stability derivatives extraction. As the input oscillations are sinusoidal, the responses are also sinusoidal, as shown in the figure.

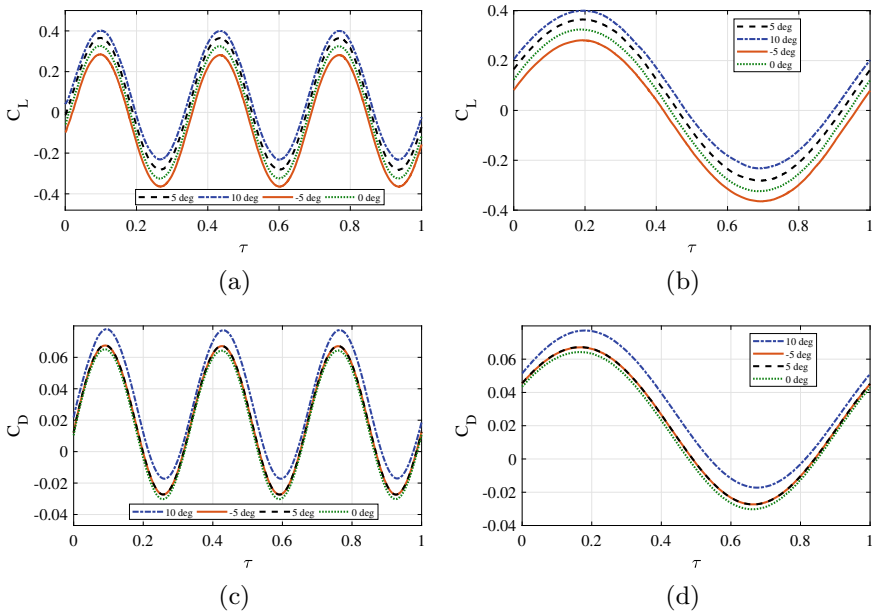


**Fig. 10** Response of Zhiyuan aerostat for **a** heave oscillation-3 cycles, **b** heave oscillation-1 cycle, **c** surge oscillation-3 cycles and **d** surge oscillation-1 cycle

The magnitude of lift increases with the increase in the angle of attack, as shown in Fig. 10a. It is due to the variation in the differential pressure between the top and the bottom surfaces of the aerostat. Further increase in the angle of attack may cause stall condition, and it is not in the scope of the current study. The drag remains constant for the smaller angles of attack, as shown in Fig. 10c, because the frontal area hit by the wind remains almost unchanged. As the angle of attack increases to  $10^\circ$ , the frontal area of the aerostat increases and the drag increases.

The stability derivatives of the Zhiyuan aerostat due to the heave oscillation were extracted using the methodology specified in Sect. 2. A comparison of the stability derivatives extracted from the surge oscillations and heave oscillations for different angles of attack are shown in Figs. 11 and 12.

Drag derivative due to axial acceleration and velocity shown in Fig. 11a, b, respectively, shows almost constant values for the small angles of attack. As the angle of attack increases to  $10^\circ$ , the derivative increases as well. This is in close agreement with the drag response shown in Fig. 10a. Lift derivative due to the axial acceleration and velocity shown in Fig. 11c, d, respectively, shows a linear variation with the angle of attack. This shows the peculiar behaviour of the aerostat to build up the lift as the axial acceleration happens, which aids the dynamic stability of the aerostat. The magnitude of the derivatives shifts from negative to positive as the angle of attack changes from negative to positive. At the zero degree angle of attack, the derivative value is close to zero. That means the acceleration of the aerostat at

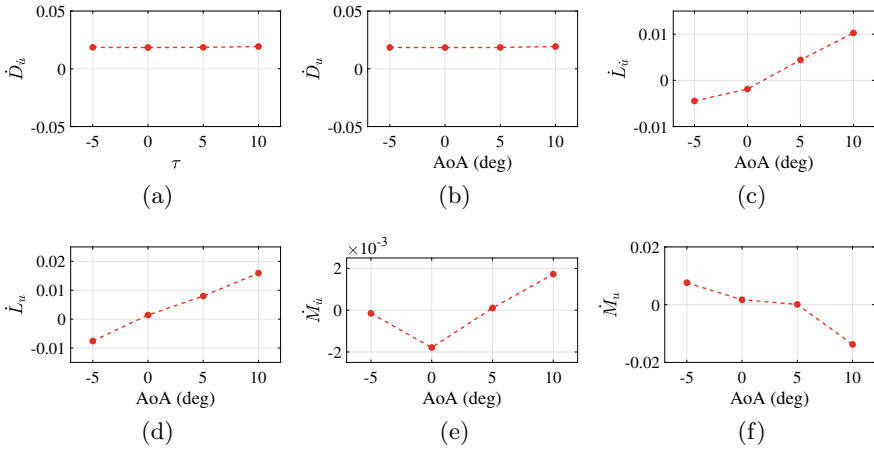


**Fig. 11** Zhiyuan aerostat stability derivatives for surge oscillations at different angles of attack

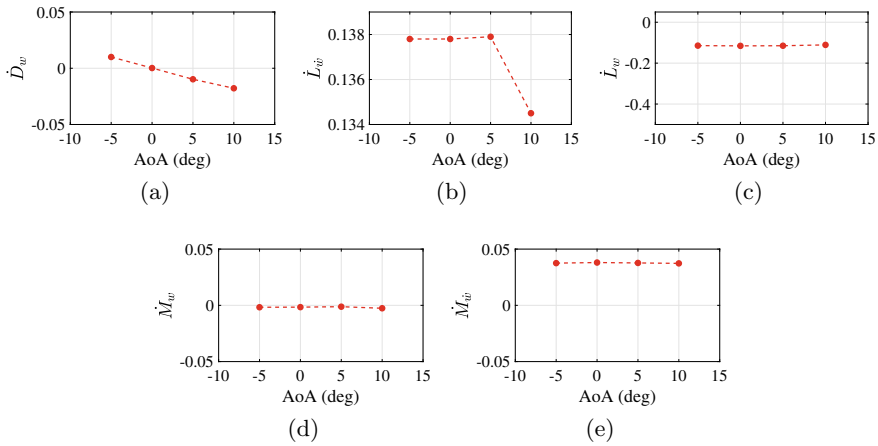


**Fig. 12** Zhiyuan aerostat stability derivatives for heave oscillations at different angles of attack

zero degrees angle of attack will not affect much on the lift. Moment derivative due to axial acceleration and velocity shown in Figs. 11e, f, respectively, show a linear decrease with the angle of attack. There is an exception at a 10° angle of attack for the acceleration derivative. Thus, the acceleration along the axial direction causes the moment to decrease, reducing the control effort for pitch control.

Drag derivative due to the vertical velocity, shown in Fig. 12a, is linearly decreasing with the angle of attack. In contrast, the lift derivative is almost constant, as shown in Fig. 12c. The lift derivative due to vertical acceleration shown in Fig. 12b remains constant for small angles of attack but reduces to a lower value for the higher angle of attack. The vertical acceleration mainly caused by vertical gusts will not aid the drag build up of the aerostat. On the other hand, it will not even benefit the

lift generation of the aerostat. The moment derivative due to vertical velocity shows a variation opposite to the moment derivative due to axial acceleration, as shown in Fig. 12c. The moment derivative due to vertical acceleration remains constant for all the angles of attack with an exception at zero degree, as shown in Fig. 12d.

## 5.6 GNVR, HAA and NPL Aerostats

The simulations for extracting the stability derivatives due to the surge and heave oscillations were repeated for the GNVR, HAA and NPL aerostats as well. Here in this section, some of those results which showed deviation from the Zhiyuan response are presented.

The response of the GNVR aerostat, HAA aerostat and NPL aerostat for surge and heave oscillations is shown in Fig. 13. A stable cycle of response used for the stability derivatives extraction is shown in the figure.

The lift response of the GNVR aerostat for different angles of attack shows an increment with the angle of attack as shown in Fig. 13a. The close similarity between the Zhiyuan shape and GNVR shape made the lift response of these two aerostats similar. The drag response of the GNVR aerostat shown in Fig. 13b has a considerable deviation from that of the Zhiyuan aerostat. Due to the more streamlined design, the Zhiyuan aerostat has a reduced drag compared to the GNVR aerostat. The lift response of the HAA aerostat for different angles of attack is shown in Fig. 13c. The amplitude of the lift increases with the increase in the angle of attack. The drag response shown in Fig. 13d demonstrates an invariant relation with the angle of attack. The moment response, shown in Fig. 13f, reduces with the increase in the angle of attack. The lift response of the NPL aerostat shown in Fig. 13e shows the least lift magnitude for the given angles of attack. The drag response remains constant for the smaller angles of attack and shows a slight increase in the magnitude for the  $10^\circ$  angle of attack, as shown in Fig. 13f. The drag magnitude is also the least among the four aerostats.

The stability derivatives obtained for the Zhiyuan aerostat is compared with those for the other aerostats, as shown in Fig. 14. The drag derivatives due to axial acceleration for the four aerostats shown in Fig. 14a remain constant with the angle of attack. Even though the individual derivatives remain constant, their magnitude varies largely among the aerostats. GNVR aerostat has the maximum value, and the NPL has the minimum value, as shown in the figure. As seen for the Zhiyuan aerostat case in Fig. 11a, the drag derivatives for the  $10^\circ$  angle of attack show a deviation for all the aerostats. It is due to the increase in the frontal area of the aerostat due to the large angle of attack. The magnitude of drag derivative for the GNVR aerostat is slightly higher than that for the Zhiyuan aerostat. This can be explained by the slightly larger diameter of the GNVR aerostat, which causes the front area to increase slightly. In a similar way, the diameter of the NPL aerostat is smaller than the Zhiyuan aerostat, which causes the front area to be smaller than the other aerostat, thereby resulting in a smaller drag. This drag magnitude pattern is reflected in the rate of change of drag

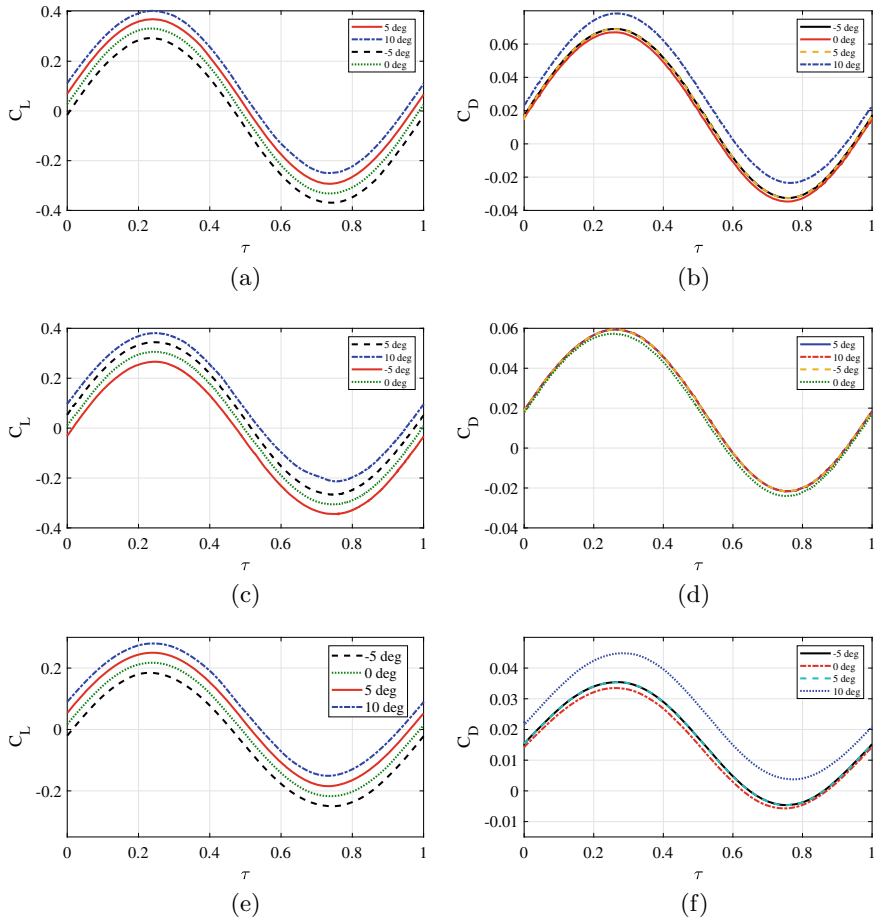


**Fig. 13** Response of GNVR aerostat for **a** heave oscillation and **b** surge oscillation, HAA aerostat for **c** heave oscillation and **d** surge oscillation, and NPL aerostat for **e** heave oscillation and **f** surge oscillation

as well. As the diameter of Zhiyuan and HAA aerostats was the same, drag response and the drag derivative remained the same, as shown in the figure. The lower drag derivative value of the NPL aerostat helps to maintain the attitude of the aerostat because as the aerostat accelerates forward, the drag build up will be comparatively less among the four aerostats. On the other hand, the other three aerostats need more station-keeping control effort.

The lift derivative due to the axial acceleration for the four aerostats is shown in Fig. 14b. There is a peculiar difference between the derivative response of the Zhiyuan aerostat among the other aerostats. As the angle of attack increases, the rate of change of lift due to the axial acceleration increases linearly, whereas the derivatives decrease for the other aerostats. This particular behaviour of the Zhiyuan



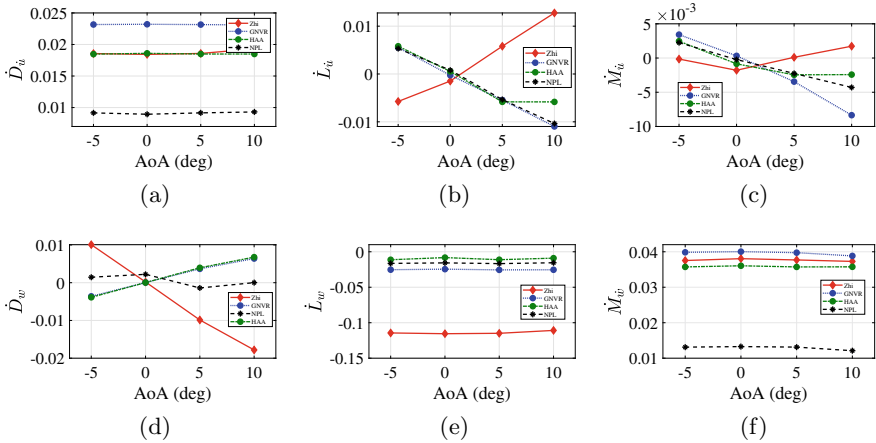


**Fig. 14** Comparing the stability derivatives of Zhiyuan aerostat with other aerostats

aerostat is advantageous for the dynamic stability of the aerostat as the increased lift helps the aerostat to be more stable. The geometry of the Zhiyuan aerostat causes this particular response. All the other aerostats considered have a less pointy leading edge than the Zhiyuan aerostat. The positive slope in the lift derivative with the axial acceleration of the Zhiyuan aerostat aids the altitude control and station-keeping control efforts. The acceleration along the axial direction causes the lift to reduce its magnitude for the other three aerostats, unlike the Zhiyuan aerostat case. It shows that the aerostat fails to retain its lift as its own. There should be control actions to maintain the required lift for the aerostat.

The moment derivatives due to the axial acceleration for the four aerostats are shown in Fig. 14c. The rate of change of moment decreases with the angle of attack for the other three aerostats. The reduction in the moment derivative due to the axial acceleration will reduce the control effort for the pitch control. The Zhiyuan aerostat moment derivative increases for the positive angle of attack, as shown in the figure. Thus, the Zhiyuan aerostat demands more control effort for maintaining the desired pitch for large positive angles of attack. Even though the stalling of the aerostat is not in the scope of this work, the pattern in the moment derivative for the Zhiyuan aerostat suggests that stalling occurs at a lower angle of attack than for the other three aerostats.

The drag derivatives due to the vertical velocity for the four aerostats are shown in Fig. 14d. There is a positive slope for the derivatives plot for the GNVR, HAA and NPL aerostats and a negative slope for the Zhiyuan aerostat. Unlike the Zhiyuan aerostat, the drag magnitude builds up as the other three aerostats accelerate in the vertical direction, primarily due to vertical wind gusts. This demands more control effort for the station keeping and attitude control for the aerostats. This shows that as the turning of the aerostat for a pitch up flight, such as taking off from the ground

station, slows down the aerostat due to the extra drag build up. The negative slope of the Zhiyuan aerostat aids the control efforts to maintain the position of the aerostat.

The lift derivatives due to the vertical velocity for the four aerostats shown in Fig. 14e possess constant values for different angles of attack. The vertical acceleration can be due to the presence of a strong vertical wind gust or an ascending flight phase at the time of the installation or maintenance of the aerostat. The Zhiyuan aerostat has the maximum lift derivative in the negative direction, which demands more control effort for the station keeping. All the other aerostats aid the lift for the ascending phase, which helps to reduce the control effort. The moment derivatives due to the vertical acceleration for the four aerostats shown in Fig. 14f also remain constant for different angles of attack. Zhiyuan, HAA and GNVR aerostats have the maximum value among the four aerostats, making the pitch control rapid and requiring more effort to keep them in the desired pitch. The NPL aerostat has the minimum value, which helps the aerostat to vary the pitch smoothly with less control effort.

## 6 Conclusions and Future Scope

The presented study has considered the translational motion of the aerostat in  $X$  (surge) and  $Y$  (heave) directions for the extraction of the stability derivative. A small-amplitude sinusoidal oscillation was used for the simulation of the aerostat motion. A methodology for the extraction of stability derivatives from the full cycle oscillation responses of the aerostat was presented with CFD simulation results. A base case aerostat shape was selected for the analysis, and three other aerostat shapes were considered for the comparison of results obtained from the analysis.

In this paper, the stability derivatives of the Zhiyuan aerostat at four different angles of attack were presented. The results of which were compared with the derivatives of the other three aerostats as well. The drag and lift performance of the Zhiyuan aerostat are superior among the four aerostats. This will help the aerostat to be controlled with less control effort during the station keeping and attitude control tasks. The NPL aerostat had better moment stability for the pitching acceleration. This will make the Zhiyuan aerostat demand more control effort for the pitching manoeuvre.

From this study, it can be concluded that the Zhiyuan aerostat can be used for the low-altitude wind measurement application. The more aerodynamic geometry of the Zhiyuan aerostat compared to the other three aerostats was the main reason for this peculiar performance. The dynamic stability analysed using the stability derivatives suggests the superiority of the Zhiyuan aerostat among the four aerostats. The drag and lift performance of the Zhiyuan aerostat are such that it aids the station keeping and attitude control efforts.

This study will be extended for the investigation of the stability derivatives due to surge and pitch motions. The longitudinal stability derivatives can be extracted from the aerostat oscillations involving the longitudinal motion variables and can be used

for the longitudinal dynamic model of the aerostat. An optimization of the aerostat geometry for improving the dynamic stability can be considered as a future direction of this study.

## References

1. Somasundaran N, Kayani V, Chandrasekhar R, Kottayil S (2019) *Int J Autom Smart Technol* 9(3). <https://doi.org/10.5875/ausmt.v9i3.1912>
2. Sengar S, Liu X (2020) *J Ambient Intell Humaniz Comput* 11. <https://doi.org/10.1007/s12652-020-01866-7>
3. Vanitha V, Raphel D, Resmi R (2019) *Innovations in power and advanced computing technologies (i-PACT)*, vol 1, pp 1–4. <https://doi.org/10.1109/i-PACT44901.2019.8960017>
4. Azad K, Alam M, Uddin S (2012) *Int J Adv Renew Energy Res* 1:48
5. Allison S, Bai H, Jayaraman B (2020) *Aerosp Sci Technol* 98:105699. <https://doi.org/10.1016/j.ast.2020.105699>
6. Anoop S, Oruganti VRM (2020) *Adv Sci Technol Eng Sys J* 5(4):167. <https://doi.org/10.25046/aj050420>
7. Anoop S, Velamati RK, Oruganti VRM (2021) *Aerosp Sci Technol* 113:106684. <https://doi.org/10.1016/j.ast.2021.106684>
8. Nguyen K, Au LTK, Phan HV, Park HC (2021) *Aerosp Sci Technol* 119:107085. <https://doi.org/10.1016/j.ast.2021.107085>
9. Bykerk T, Verstraete D, Steelant J (2020) *Aerosp Sci Technol* 98:105709. <https://doi.org/10.1016/j.ast.2020.105709>
10. Jones SP, DeLaurier JD (1983) *J Aircr* 20(2):120. <https://doi.org/10.2514/3.44840>
11. Badesha S (1993) 10th lighter-than-air systems technology conference, pp 1–4. <https://doi.org/10.2514/6.1993-4036>
12. Ignatyev DI, Khrabrov AN (2015) *Aerosp Sci Technol* 41:106. <https://doi.org/10.1016/j.ast.2014.12.017>
13. Waqar A, Ali OA, Erwin S, Mohamed AJ (2017) *Aircr Eng Aerosp Technol* 89:174. <https://doi.org/10.1108/AEAT-06-2015-0165>
14. Tao Q, Tan TJ, Cha J, Yuan Y, Zhang F (2021) *Unmanned Sys* 09(01):73. <https://doi.org/10.1142/S2301385021500060>
15. Junior JLM, Santos JS, Morales MA, Goes LC, Stevanovic S, Santana RA (2019) *AIAA Aviation Forum*. <https://doi.org/10.2514/6.2019-2982>
16. Wang XL (2012) *J Aircr* 49(3):933. <https://doi.org/10.2514/1.C031634>
17. Ronch AD, Vallespin D, Ghoreyshi M, Badcock KJ (2012) *AIAA J* 50(2):470. <https://doi.org/10.2514/1.J051304>
18. Ronch AD (2012) *On the calculation of dynamic derivatives using computational fluid dynamics*. Ph.D. thesis, University of Liverpool
19. Carrión M, Biava M, Barakos GN, Stewart D (2017) *J Aircr* 54(4):1328. <https://doi.org/10.2514/1.C033987>
20. Lee SK, Joung TH, Cheo SJ, Jang TS, Lee JH (2011) *Int J Nav Archit Ocean Eng* 3(3):174. <https://doi.org/10.2478/IJNAOE-2013-0060>
21. Mader CA, Martins JRRA (2014) *AIAA J* 52(11):2533. <https://doi.org/10.2514/1.J052922>
22. Bykerk T, Verstraete D, Steelant J (2020) *Aerosp Sci Technol* 103:105883. <https://doi.org/10.1016/j.ast.2020.105883>
23. Muller L, Libsig M, Martinez B, Bastide M, Bidino D, Yannick B, Roy JC (2020) *AIAA Aviation Forum*. <https://doi.org/10.2514/6.2020-2782>
24. Javanmard E, Mansoorzadeh S, Mehr JA (2020) *Ocean Eng* 215:107857. <https://doi.org/10.1016/j.oceaneng.2020.107857>

25. Ghoreyshi M, Jirásek A, Cummings RM (2014) Prog Aerosp Sci 71:167. <https://doi.org/10.1016/j.paerosci.2014.09.001>
26. Kale S, Joshi P, Pant R (2005) AIAA 5th ATIO and 16th lighter-than-air system technologies and balloon systems conferences. <https://doi.org/10.2514/6.2005-7442>
27. Liang H, Zhu M, Guo X, Zheng Z (2012) 50h AIAA aerospace sciences meeting including the New Horizons forum and aerospace exposition. <https://doi.org/10.2514/6.2012-1180>
28. Yang Y, Xu X, Zhang B, Zheng W, Wang Y (2020) Aerosp Sci Technol 98:105664. <https://doi.org/10.1016/j.ast.2019.105664>
29. Wang QB, Chen JA, Fu GY, Duan DP (2009) J Zhejiang Univ Sci A Appl Phys Eng 10:1609. <https://doi.org/10.1631/jzus.A0820814>
30. Khoury G (2012) Airship technology. Cambridge University Press, Cambridge
31. Ansys (2020) Academic research FLUENT, release 20.2, Help system, fluent theory manual. Guide. ANSYS, Inc., Canonsburg, PA, USA
32. Compendium of unsteady aerodynamic measurements. AGARD-R-702. Report (Aug 1982)
33. Korotkin A (2009) Added masses of ship structures, vol 88. <https://doi.org/10.1007/978-1-4020-9432-3>